



Strategy for improving the visible photocatalytic H₂ evolution activity of 2D graphitic carbon nitride nanosheets through the modification with metal and metal oxide nanocomponents



Rama Krishna Chava*, JeongYeon Do, Misook Kang*

Department of Chemistry, College of Natural Sciences, Yeungnam University, 280 Daehak-Ro, Gyeongsan, Gyeongbuk, 38541, Republic of Korea

ARTICLE INFO

Keywords:

g-C₃N₄ nanosheets
Au NPs
In₂O₃
Nanoternary composite
Photocatalytic H₂ evolution

ABSTRACT

The semiconductor based photocatalytic water splitting is a promising approach for the production of environmentally friendly, clean, and cost-effective hydrogen fuel by utilizing the solar energy. Graphitic carbon nitride (g-C₃N₄) has emerged as an excellent material to produce hydrogen via photocatalytic water splitting reactions, however the limited visible light absorption and fast charge recombination restricts the further real practical applications. Fabrication of multicomponent g-C₃N₄ based heterostructured photocatalytic system is an effective strategy to enhance the charge separation and thereby photocatalytic efficiency. Here, a new g-C₃N₄-Au-In₂O₃ ternary system with efficient photogenerated charge carrier separation is successfully designed. The morphology, structure, phase and electronic environments of g-C₃N₄, Au and In₂O₃ in the composite were studied by different characterization methods. As expected, the optimized g-C₃N₄-Au-In₂O₃ catalyst shows excellent photocatalytic H₂ evolution rate. The improved photocatalytic H₂ evolution rate could be attributed to the formation of heterojunctions between g-C₃N₄, Au and In₂O₃ components; improved visible light harvesting via surface plasmon resonance (SPR) effect of metal Au nanoparticles (NPs); and effective photogenerated electron-hole pairs separation. The proposed work is expected to provide a new concept to fabricate g-C₃N₄ based ternary heteronanostructures with metal NPs and metal oxide semiconductors not only to a photocatalytic applications but also opens up to variety of optoelectronic applications.

1. Introduction

Photocatalytic water splitting for hydrogen (H₂) production is one of the most promising methods, in which direct sunlight can be used for producing hydrogen as a green fuel. Ever since the development of photocatalytic water splitting reaction on the surface of TiO₂ photocatalyst material [1], several efforts have been proposed for the development of new materials that are capable of harvesting the solar energy and to convert it into the chemical hydrogen [2–4]. However, the major problems to realize high photocatalytic activity from solar radiation are poor visible light absorption and rapid electron-hole recombination processes [5]. An optimal photocatalyst sample should possess some qualities toward efficient hydrogen production: a lower bandgaps that absorbs the light in the entire visible region, efficient photoexcited charge carriers' migration and separation, fast reactions at solid-liquid interfaces, and stable during the contact with aqueous solutions. Furthermore, it should be non-toxic, earth abundant, and easily processable [6–8]. The rapid electron-hole recombination rates lead to

a lower efficiency of photocatalysts which plays a critical role in the final photocatalytic efficiency of a whole system. In the last decades, various organic and inorganic semiconductors have been designed for photocatalytic hydrogen production [4,6,9–13].

Recently, g-C₃N₄ (CN), has been emerged as a star material for photocatalytic H₂ evolution owing to its suitable bandgap (≈ 2.7 eV), low cost, excellent chemical stability and nontoxicity [14–16]. Even though, the photocatalytic H₂ evolution from g-C₃N₄ material has achieved certain results, the pure g-C₃N₄ suffers high electron-hole recombination, insufficient light absorption and poor charge transport properties which results the low performance towards H₂ production [17–19]. For this purpose, various structural and morphological modifications have been suggested to increase the photocatalytic water splitting reactions. Amongst them, loading of noble metal nanoparticles [20,21], doping [22–26], morphological modifications [27–29], surface modifications [30–34] resulting in the band gap narrowing, modification of electronic properties, and thus in improved photocatalytic water splitting performances. Wang et al, synthesized boron modified g-C₃N₄

* Corresponding authors.

E-mail addresses: rama@ynu.ac.kr, drckphysics@hotmail.com (R.K. Chava), mskang@ynu.ac.kr (M. Kang).

nanosheets in which the inter-layer distance was successfully decreased and improved surface reactivity towards higher photocatalytic H₂ evolution was observed [35]. In other case steam reforming strategy was introduced for the fabrication of two dimensional carbon nitride nanosheets with more reaction sites, extended electron lifetime and higher charge separation efficiency which in turn produced the excellent photocatalytic H₂ evolution activity [36,37]. Thermal oxidation etching process was coined by Ping et al, in which two nanometer sized g-C₃N₄ nanosheets were obtained with high surface area, larger bandgap, increased life time of photogenerated charge carriers, higher electron transport. As a result, superior photocatalytic activities were observed in comparison to bulk g-C₃N₄ [38]. Sun, et al and Dandan, et al designed hollow graphitic carbon nitride spheres with efficient light harvesting capacity, spatially separated reactive sites for H₂ evolution reactions [39,40]. Some other efforts consist of making g-C₃N₄ heterostructures with other semiconductors or loading of cocatalysts on to g-C₃N₄ surface for improving the visible light absorption, and charge separation efficiency. These semiconductors include TiO₂ [41], α-Fe₂O₃ [42], ZnS [43], CdS [44], Ni₃C [45], Ba₅Ta₄O₁₅ [46], NaNbO₃ [47], CoP [48], CuS [49], NiS [50], etc. However their real-world applications are restricted due to insufficient visible light absorption and low quantum efficiency. Hence, it is still of great attention to develop a highly active g-C₃N₄ based photocatalytic system towards largescale photocatalytic H₂ production.

Noble metal NPs (Au and Ag) have been documented as an active media for harvesting the solar energy benefitting from their localized surface plasmon resonance (SPR) effect. The SPR induced hot plasmon electrons can boost the visible light absorption capability of semiconductors. In addition to this, these noble metal nanoparticles (NPs) form a Schottky barrier with the semiconductor which can effectively captures the photoexcited electrons and thereby increases the charge carrier separation. Accordingly these noble metals will act as active sites for H⁺ reduction [51].

Another way to improve the photocatalytic H₂ evolution activity of g-C₃N₄ is to construct heterojunctions with metal oxides such as TiO₂, SnO₂, ZnO. The obtained proper level platform can stimulate the photogenerated charge carriers migration and separation. Consequently, the photocatalytic activity for H₂ evolution, CO₂ conversion, and dye degradation of g-C₃N₄ could be considerably improved [51–55]. Therefore, it is a viable approach to improve the photocatalytic H₂ evolution activity of g-C₃N₄ by combining a dual functional noble metal modification and then proper metal oxide semiconductor hybridization towards effective charge transfer and separation. The proposed strategy is much favourable to construct the heterojunctions with g-C₃N₄ to concurrently modify the photogenerated electrons and holes for efficient photocatalytic H₂ evolution activity.

Based on the above considerations and scarce reports on the designed strategy, in this work we have developed a g-C₃N₄-Au-In₂O₃ (CN-Au-IO) ternary photocatalytic system for H₂ evolution reaction. Here, In₂O₃ is an n-type metal oxide semiconductor with a bandgap of ≈ 2.8 eV and most stable at ambient environments. Since both the valence band and conduction bands of In₂O₃ are lower than those of g-C₃N₄, hence there is a possibility to make the g-C₃N₄-In₂O₃ heterojunctions with effective interfacial electron transfer processes toward efficient photocatalytic H₂ generation. In this work, we have concentrated on the basic mechanisms of heterojunctions formation, charge transfer and migration, and optical properties in g-C₃N₄-Au-In₂O₃ heteronanostructures. In addition to this, the effect of Au NPs content on the morphological, structural and photocatalytic H₂ evolution activities were also clearly investigated and discussed.

2. Experimental section

2.1. Synthesis of g-C₃N₄ nanosheets (CNNSs)

The CN nanosheets were synthesized by a thermal polymerization of

melamine precursor in the presence of NH₄Cl [56]. At first, 20 g of melamine was thoroughly mixed with 3 g of NH₄Cl for 0.5 h. Then the mixture was transferred to a crucible with lid and then heated at 550 °C for three hours at a heating rate of 1 °C/min. After cooling down, the obtained light yellow powder was finely grounded in a mortar and stored at room temperature.

2.2. Synthesis of Au NPs

The spherical shaped Au metal NPs with a ≈ 15 nm diameter were synthesized by our previous reported method [57]. Pre-calculated HAuCl₄ content was dissolved in 100 ml DI water and boiled under mild stirring. Next, 5 ml of Na₃Cit solution (34 mM) was added at once and keep on stirring. With constant stirring, the solution was changed from colorless to red colour after 15 min forming the citrate stabilized Au NPs.

2.3. Synthesis of g-C₃N₄-Au (CN-Au) nanostructures

For the preparation of CN-Au nanostructures, 20 mg of CN nanosheets was mixed with 30 ml DI water with sonication and stirring. After being stirred for 30 min, 5 ml of Au NPs solution was added dropwise and kept stirring for another 30 min. Then the mixed solution was treated at 140 °C for 12 h via a hydrothermal process. The obtained sample was washed with distilled water and dried at 60 °C for overnight and termed as CN-5Au. In addition to this, 7 ml and 10 ml Au NPs containing g-C₃N₄ nanostructures were also prepared in same manner and denoted as CN-7Au and CN-10 Au respectively.

2.4. Synthesis of g-C₃N₄-Au-In₂O₃ heteronanostructures (CN-Au-IO HNSs)

For CN-7Au-IO HNSs preparation, 20 mg of CNNSs was dispersed in 20 ml DI water with rigorous stirring and ultrasonication. After that 7 ml of above prepared Au NPs solution was added and stirred for another 10 min. Next, a 52 ml solution containing 2 mM tri sodium citrate, 2.4 mM InCl₃ and 2 mM urea was added dropwise and kept on stirring for another 0.5 h. Subsequently, the obtained solution was changed to Teflon liner and treated at 140 °C for 12 h. After cooling down, the precipitate was washed and dried at 60 °C for overnight. Next, the obtained sample was calcined at 350 °C for 2 h. Other samples with 5 and 10 ml Au NPs were also prepared in the same manner. As per Au content, samples were named as CN-5Au-IO, CN-7Au-IO and CN-10Au-IO. For comparison, In₂O₃ (IO) and g-C₃N₄-In₂O₃ (CN-IO) nanostructures were also prepared without the addition of Au NPs. Based on theoretical calculations, the weight ratios of CN:Au:In₂O₃ in a final composite CN-7Au-IO is 1:0.06:0.87.

2.5. Physical characterization of samples

FE-SEM images were taken from HITACHI made S-4800 system. Low and high resolution TEM images were received from HITACHI made H-7600 TEM and Titan G2 FE-TEM instrument respectively. X-ray diffraction (XRD) profiles were checked on Panalytical Xpert Pro diffractometer (Cu-Kα, $\lambda = 1.54060$ Å). X-ray photoelectron spectroscopy (XPS) measurements were performed on Thermo-Scientific X-ray photoelectron spectroscope instrument. Samples were fixed using a double sided tape and all elements were standardized by the binding energy of C-1s(284.6 eV). For all analyses, monochromatic Al-Kα radiation was used. A flood gun with variable emission current and variable electron voltage was used for charge compensation. The peak positions were determined with a precision of ± 0.1 eV. All measurements were executed in an ultrahigh vacuum (UHV) experimental chambers operating at base pressures $< 10^{-10}$ mbar. Nitrogen adsorption and desorption isotherms were recorded on a Belsorp-mini II (MicrotracBEL Corp., Japan) instrument operating at an adsorption temperature of

77 K. Before N_2 adsorption and desorption measurements, sample was pretreated at 150 °C for 2 h. UV-VIS spectra were collected using Scinco spectrophotometer and photoluminescence spectra were taken on Scinco spectrofluorometer at $\lambda_{exc} = 390$ nm.

2.6. Photocatalytic hydrogen evolution details

The photocatalytic H_2 evolution activities of as obtained samples were estimated by the visible photocatalytic hydrogen evolution reaction in a Pyrex side irradiation vessel. In a typical photocatalytic experiment, 10 mg of catalyst sample was dispersed in 50 ml aqueous methanol solution (10 vol% methanol) as sacrificial reagent. Prior to the experiment, the reaction solution was N_2 flushed to remove the dissolved oxygen. The solution was irradiated by a simulated solar-light irradiation (150 W Xenon lamp, $\lambda \geq 420$ nm). The produced gas was examined by gas chromatography fitted with a thermal conductivity detector using high-purity argon carrier gas. The stability of optimized photocatalysts samples was measured up to 7 cycles and each cycle includes four hours. The apparent quantum efficiency (AQY) of optimized photocatalyst sample was calculated from the following equation and the complete parameters were given in supporting information.

$$\eta AQY = 2 \times \frac{\text{amount of hydrogen gas molecules evolved}}{\text{number of incident photons}} \times 100\% \quad (1)$$

2.7. Photocurrent and electrochemical impedance spectroscopy (EIS) measurements

The transient photocurrent profiles were recorded using an IVIUM STAT electrochemical setup with standard three electrode system in which the sample deposited on substrate acts as working electrode, Ag/AgCl as a reference electrode, and Pt wire used as a counter electrode. A light source with emitting radiation wavelength $\lambda > 420$ nm was employed for measurements. Aqueous Na_2SO_4 (0.5 M) solution was used for electrolyte purpose. The EIS spectra were taken at a frequency ranging from 0.01 Hz to 100 kHz with modulation amplitude of 5 mV. In these measurements, working electrode was prepared by mixing the 50 mg of photocatalyst sample with 0.5 ml DI water and 0.5 ml ethanol and then sonicated successively for 1 h. The obtained paste was made into film on FTO glass substrate using doctor blade method. The obtained films were calcined at 300 °C.

3. Results and discussions

3.1. Structural and morphological analysis

The phase purity of CN, IO, and CN-Au-IO photocatalyst samples are studied by X-ray diffraction patterns. As seen in Fig. S1, the pure $g-C_3N_4$ nanosheets exhibited a diffraction peak centered at 27.73° which corresponds to (002) plane and associated with the stacking of graphitic layers which give an interplanar distance [44,45,58]. For the pure In_2O_3 , six characteristic peaks observed at 21.41°, 30.55°, 35.30°, 45.77°, 50.98°, and 60.71° which were belong to the (211), (222), (400), (431), (440), and (622) planes respectively assigned to In_2O_3 cubic phase (JCPDS No.: 01-071-2195). For the CN-IO composite, all the representative peaks assigned to cubic In_2O_3 and $g-C_3N_4$, and confirms the purity of samples. In addition to this, XRD patterns of CN-Au composites are also recorded and are shown in Fig. S1. From Fig. S1, CN-Au composite displayed only two phases of cubic Au and $g-C_3N_4$.

Next, powder XRD patterns of final materials, CN-Au-IO nanocomposites were also recorded and are given in Fig. 1. All patterns given in Fig. 1 exhibited the diffraction planes of $g-C_3N_4$, Au and In_2O_3 . As the amount of Au content is increased, the intensity and number of Au diffraction planes also increased. The diffraction planes observed at 38.13°, 44.36°, 64.57° and 77.65° are the characteristic planes of (111), (200), (220), and (311) respectively. All these diffraction planes were

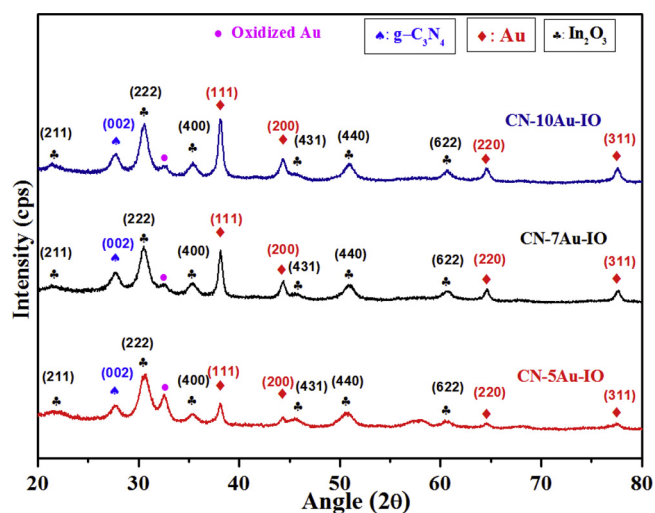


Fig. 1. Powder X-ray diffraction patterns of CN-Au-IO photocatalyst samples.

indexed to the standard JCPDS No: 01-089-1697 of cubic Au. It is also observed that when compared to pure $g-C_3N_4$ there is a slight shift towards higher angles in (002) plane after making heteronanostructures with Au and In_2O_3 . This shift may be due to the nitrogen defects caused in a narrowing interlayer distance [59,60]. Moreover, the (111) diffraction of Au becomes sharper with the increase of Au contents, indicating that the particle size of Au nanoparticles increased slightly. In addition to these features, an extra diffraction peak is also observed at $2\theta = 32.57^\circ$ which is the characteristic of oxidized Au according to the standard JCPDS No: 00-023-0278. The oxidation of Au NPs occurred in the process of calcination. These observations suggest that $g-C_3N_4$ could act as an excellent substrate to anchor Au and In_2O_3 NPs.

The surface morphology of all synthesized samples is investigated by FE-SEM images in each stage and provided in Fig. 2. Fig. 2a–c depicts the formation of CN-IO nanocomposites in which In_2O_3 nanospheres are successfully grown on the surface $g-C_3N_4$ nanosheets. As shown in Fig. 2d–f, the $g-C_3N_4$ -Au nanocomposites in which Au NPs are evenly distributed on to $g-C_3N_4$ nanosheets. Next, the final composite CN-7Au-IO was shown in Fig. 2g–i, in which both Au NPs and In_2O_3 nanospheres are successfully anchored on the surface of CN nanosheets. For comparison, also checked the images of pure In_2O_3 and found to be they are formed as spherical structures with 100 nm size. Elemental and composition details of prepared samples were checked by recording the EDS and elemental mapping profiles (Figs. S2 and S3), which further confirmed that CN-IO consists of only C, N, In and O elements and whereas the CN-7Au-IO nanocomposite consists of C, N, Au, In and O elements with their respective compositions. To further elucidate the microscopic morphology evolution, TEM images also have been taken. As depicted in Fig. 3a–b, the pure CN exhibit a stacking structure with folded edges. Fig. 3c displays the as synthesized citrate stabilized Au nanoparticles having a diameter of ~15 nm. As seen in Fig. 3d–f, CN-IO composite consists of spherical In_2O_3 nanostructures were deposited on the surface of CNNSs during the hydrothermal method. Moreover, Fig. 3g–i represents the TEM images of CN-7Au-IO nanocomposites in which both Au NPs and In_2O_3 spheres are clearly distinguished. From SEM and TEM measurements, it is confirmed that CN-7Au-IO nanocomposites were successfully prepared and also found that the Au and In_2O_3 components were well-dispersed on the surface of CN nanosheets. The proposed heterostructures can offer more reaction sites for efficient charge separation and then enhancing the photocatalytic activity of the final nanocomposite. To validate the interfacial contacts of the Au and In_2O_3 components on the surface of CN nanosheets, HR-TEM image was also taken. Fig. 4a displays legible lattice fringes and the interplanar lattice spacing is established as 0.28 nm which is associated with the (222) plane of cubic In_2O_3 . The lattice spacing of 0.24 nm is

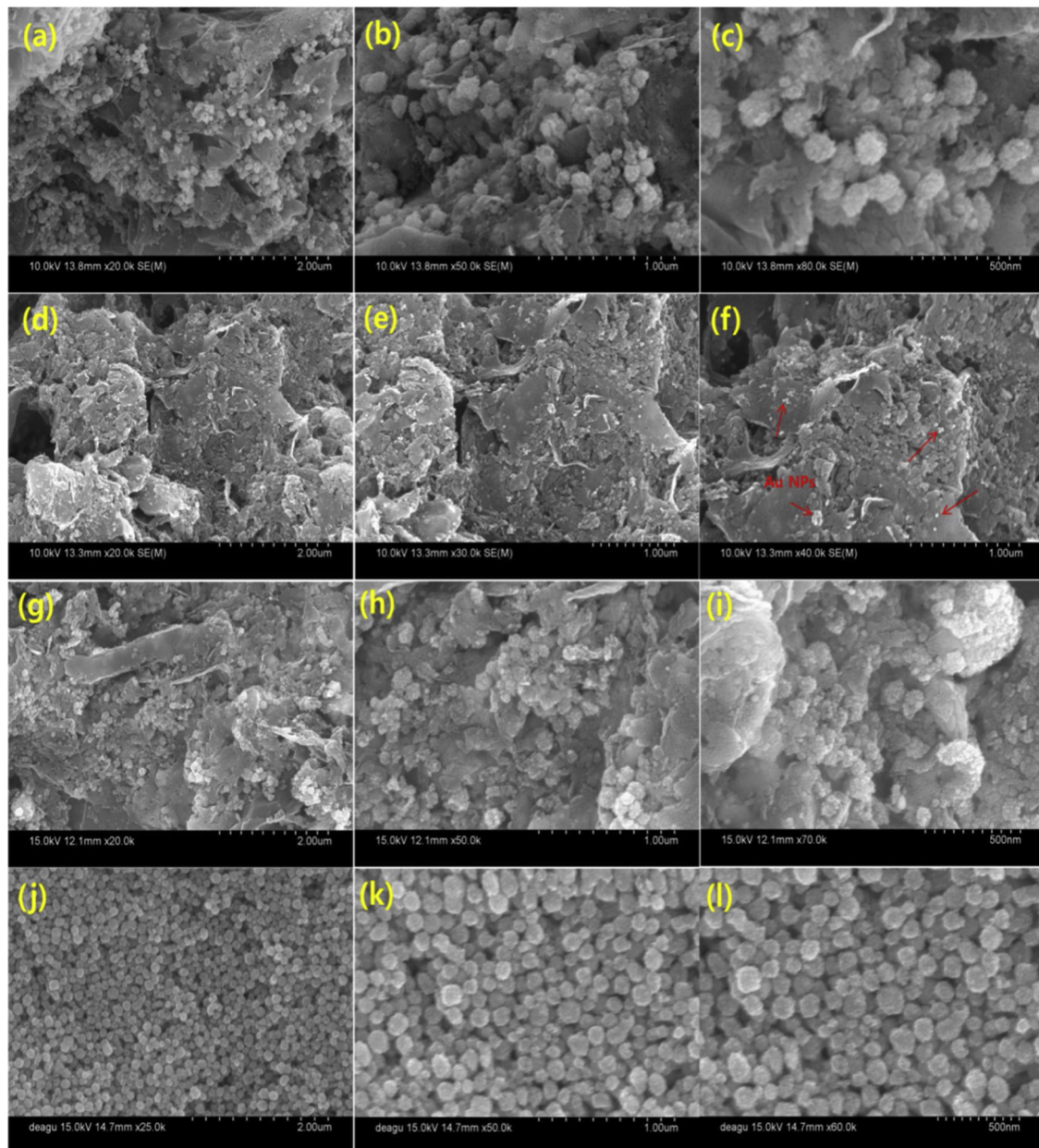


Fig. 2. FE-SEM images of (a–c) CN-IO, (d–f) CN-Au, (g–i) CN-7Au-IO heterostructures and (j–l) In_2O_3 nanospheres at different magnifications.

characteristic of cubic Au (111) plane. The SAED patterns given in Fig. 4b consisting of bright circular rings confirms that the dispersed In_2O_3 nanoparticles possess crystalline in nature and the observed rings are assigned to the different diffraction planes. Since the Au and In_2O_3 nanoparticles are distributed on $\text{g-C}_3\text{N}_4$ nanosheets, EDX scanning and mapping analyses are carried out to explore the specific distributions of the elements. As shown in Fig. 4c–i, the EDX mapping profiles further confirmed that the CN nanosheets are composed of C and N elements, Au and In_2O_3 NPs uniformly dispersed on the $\text{g-C}_3\text{N}_4$ nanosheets surface.

To examine the chemical states and oxidation states, the XPS measurements were carried out. As seen from the Fig. 5a, the surface scan spectrum of CN-7Au-IO nanocomposite exhibited C, N, Au, In and O elements with atomic weight percentages of 33.19, 42.92, 0.6, 7.67 and 15.61% respectively. In the C-1 s spectrum (Fig. 5b), the BE values observed at 284.63 eV and 288.21 eV are attributed to sp^2 hybridized C–C bonding and carbon in N–C = N aromatic rings, respectively [61,62]. A small deconvoluted peak at 289.75 eV is ascribed to C–O

bonds due to the oxygen adsorbed on the surface [63]. Fig. 5c displays the deconvoluted N1s XPS spectrum which exhibited three binding energy peaks at 398.35, 400.6, and 404.1 eV. The strongest peak at 398.35 eV was originated from sp^2 bonded N in C–N = C aromatic rings. The peak at 400.6 eV specified the existence of amino groups (C–N–H) and the other peak at 404.10 was assigned to positive charge localization and charging effects in heterocycles [35,64,65]. Fig. 5d, shows the XPS spectrum of In-3d core level. The peaks centered at 444.40 and 451.95 eV can be assigned to $\text{In3d}_{5/2}$ and $\text{In3d}_{3/2}$ signals respectively. The symmetric peak shape specifies the oxidation states and indicates that indium is trivalent in the oxide form [57,66]. The spin-orbit splitting between In 3d_{5/2} and In 3d_{3/2} regions is 7.6 eV and the existence of satellite peaks in the spectrum specifies the normal state of In^{3+} in the prepared photocatalysts sample. As shown in Fig. 5e, high-resolution O1s XPS spectrum can be fitted into two peaks with the BE values of 529.45 and 531.75 eV which were allocated to lattice oxygen atoms in In_2O_3 and surface adsorbed hydroxyl groups respectively [67,68]. Further, as seen from Fig. 5f, Au-4f exhibited the

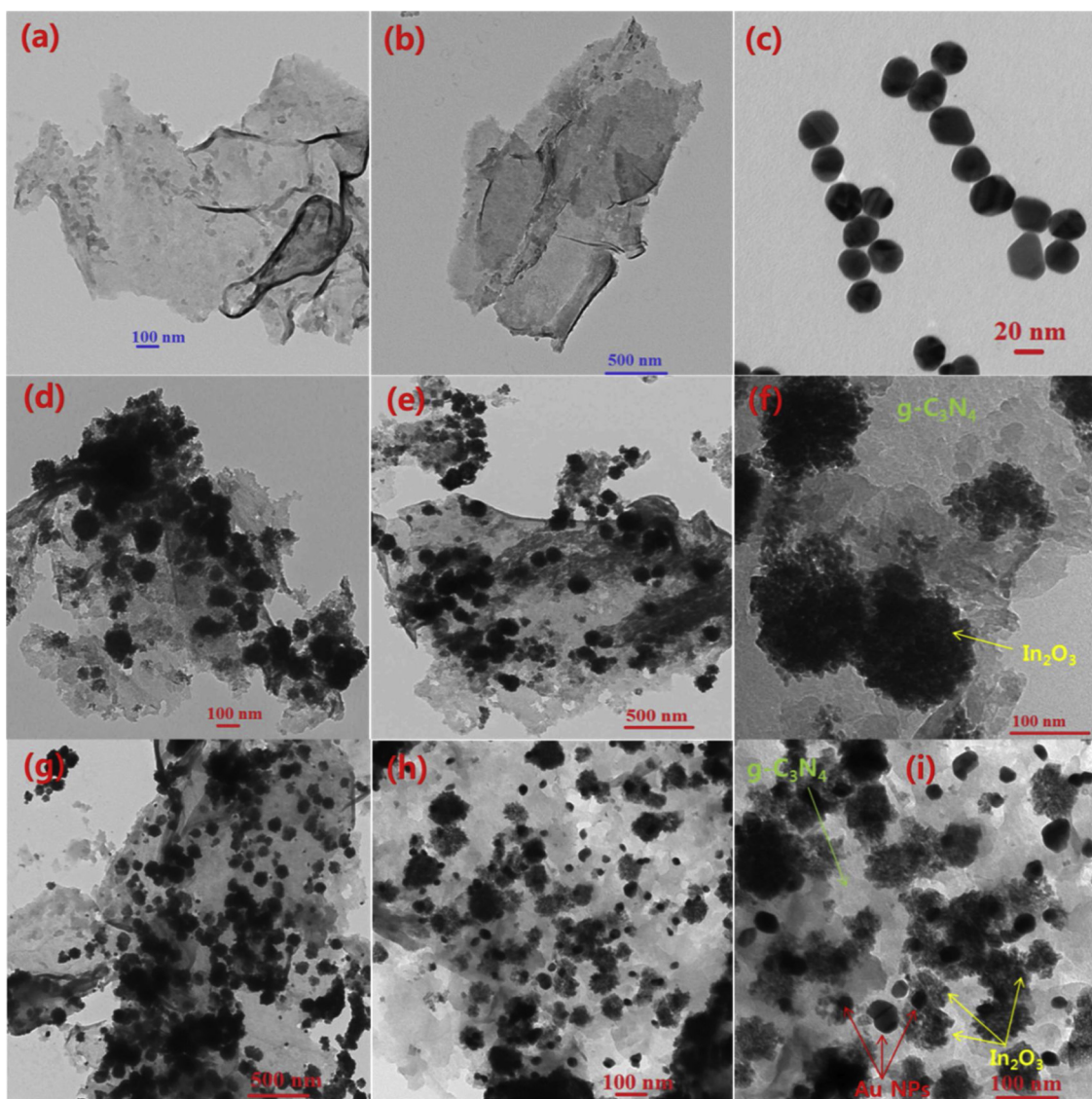


Fig. 3. TEM images of (a,b) $g\text{-C}_3\text{N}_4$ nanosheets, (c) Au nanoparticles, (d-f) CN- In_2O_3 and (g-i) CN-7Au-IO heterostructures.

bands related to metallic and as well as oxidized Au states. The peaks observed at 83.22 eV and 86.68 eV were assigned to Au metallic state (Au^0). Another peak detected at 89.68 eV is in accordance with the oxidized gold species, Au^{3+} [69,70] which is also detected in XRD patterns. From these data, CN-7Au-IO samples verify the successful decoration of Au and In_2O_3 NPs.

3.2. BET surface area and pore-size distribution studies

N_2 adsorption and desorption curves were recorded to determine the BET surface areas and pore-size distribution details. Fig. 6a depicts the N_2 adsorption-desorption isotherms of CN, CN-IO and CN-Au-IO samples. As seen from Fig. 6, all adsorption-desorption isotherms display typical type III isotherms having type H3 hysteresis loops representing the mesoporous character of the prepared photocatalyst samples. In addition to this, the pore-size distributions of CN, CN-IO and CN-Au-IO samples were also measured and the corresponding wide range distributions from 2 to 100 nm reveal that the prepared samples consist of mesopores and macropores (Fig. 6b). Table 1 displays the BET surface area and pore size distributions of all photocatalyst samples, and it can be seen that pure CN showed a surface area of $84.87 \text{ m}^2/\text{g}$ and where as the CN-IO sample showed a significant decrease in surface

area ($38.18 \text{ m}^2/\text{g}$). This decrement is due to the blocking or filling effect of deposited In_2O_3 nanospheres on the surface of CN. However, after loading of Au NPs and In_2O_3 nanospheres on the surface of CN, the surface area values were dramatically increased to 138.26, 137.40, and $136.28 \text{ m}^2/\text{g}$ for CN-5Au-IO, CN-7Au-IO, and CN-10Au-IO respectively. The presence of Au NPs, and In_2O_3 nanospheres on CN nanosheets might be the reason for improved surface area. It is well established that the photocatalyst samples with higher surface area can accommodate more active reactants and species on its surface, which in turn improves the photocatalytic activities.

3.3. Optical properties

The optical properties of as prepared photocatalyst samples were determined using UV-vis absorption spectroscopy. Fig. 7a shows the optical absorption spectra of $g\text{-C}_3\text{N}_4$ nanosheets, CN-Au-IO and CN-IO composites. The $g\text{-C}_3\text{N}_4$ is capable of absorbing visible light since it has the absorption until 500 nm. When coupling $g\text{-C}_3\text{N}_4$ and with In_2O_3 , this binary compound shows blue shifted absorption edge relative to pure $g\text{-C}_3\text{N}_4$. As expected, g-CN-Au-IO photocatalysts showed improved visible light absorption when compared to CN and CN-IO. This improved visible light absorption is contributed from Au NPs which

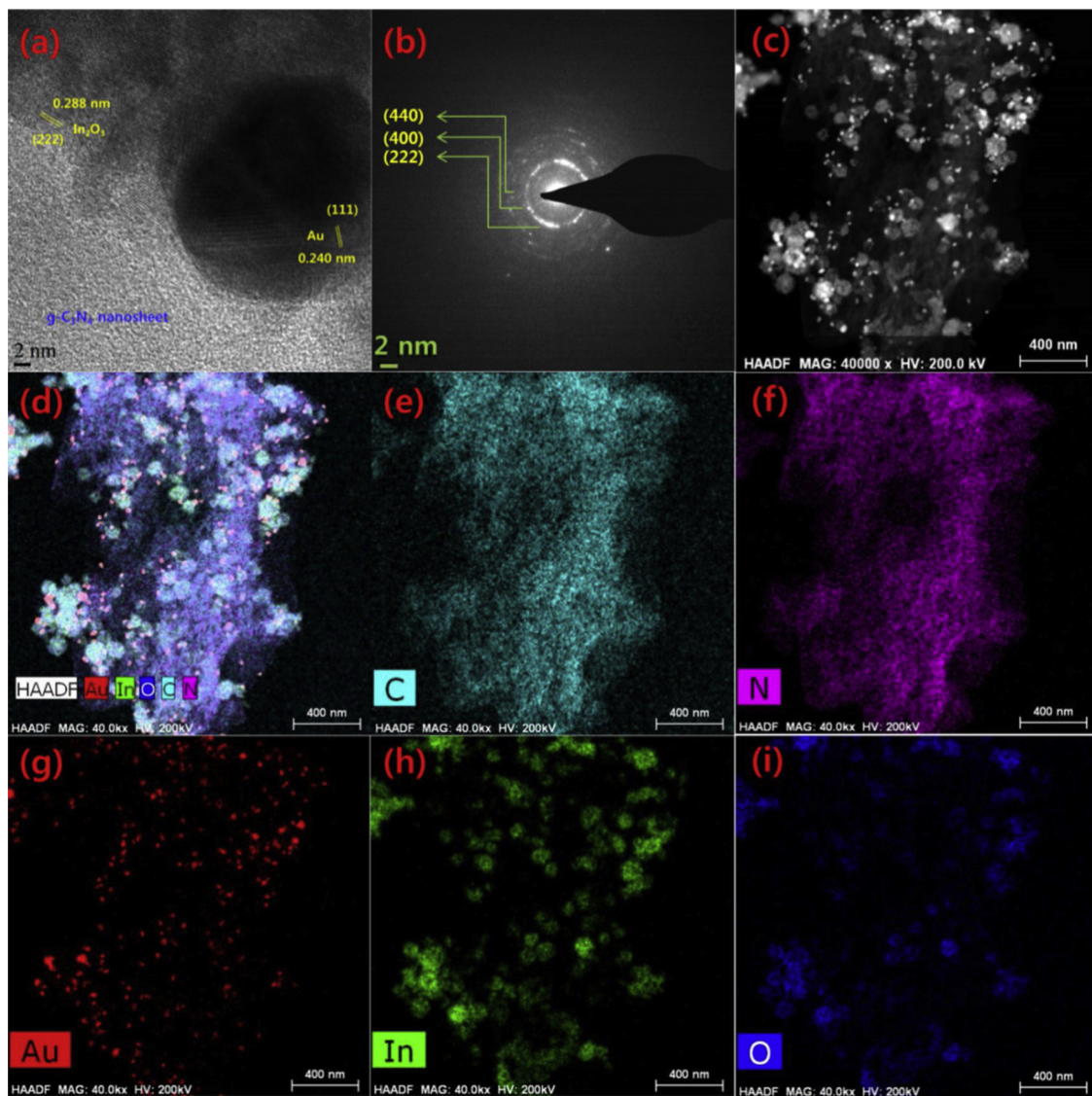


Fig. 4. HR-TEM image (a) showing lattice spacings, (b) SAED patterns, (c) STEM and (d-i) STEM-EDS elemental mapping profiles of CN-7Au-IO heterostructures.

exhibited a characteristic surface plasmon resonance (SPR) peak around 550 nm. The SPR peak of CN-Au-IO photocatalysts shown redshifted with the increase of Au NPs content and optimized at 7 ml Au content in the CN-IO composite. From the corresponding Tauc plot and by using Kubelka–Munk formula, the average bandgap values were measured and given in Fig. S4. Improved light harvesting nature was observed when increasing the relative amounts of Au NPs. These results further confirmed that Au and In_2O_3 NPs are successfully deposited on the surface of $\text{g-C}_3\text{N}_4$ nanosheets.

Photoluminescence spectral analysis was utilized to probe the transfer, migration, and separation efficiency of the photogenerated electron-hole pairs in the prepared samples [71]. As seen from Fig. 7b, pure CN nanosheets sample exhibited strong emission at 470 nm. The CN-Au-IO nanocomposites exhibit a similar PL spectrum with much weaker intensity compared to CN nanosheets and CN-IO composite, in which CN-7Au-IO exhibits the lowest PL intensity, confirming excellent charge separation efficiency and the probable optimum photoactivity. The decreased PL intensity in CN-7Au-IO photocatalyst sample could be assigned to the lower electron-hole recombination rate and finally contribute to higher photocatalytic activities.

3.4. Visible photocatalytic H_2 evolution measurements

The photocatalytic H_2 evolution activity of various samples were evaluated in the presence of 10% methanol aqueous solution under the visible light irradiation ($\lambda \geq 420$ nm). As shown in Fig. 8a, CN nanosheets produced a low H_2 evolution rate of $21.45 \mu\text{mol.h}^{-1}$, owing to the rapid recombination of electrons and holes. After loading Au NPs onto CN nanosheets it is evident that the visible light photocatalytic H_2 evolution rates of CN-Au nanostructures is significantly improved when compared to that of CN nanosheets. The amounts of H_2 gas produced from CN containing different amounts of Au are 25.72, 29.21, and $24.63 \mu\text{mol.h}^{-1}$ for CN-5Au, CN-7Au, and CN-10Au respectively. The H_2 evolution rates were increased with the increase of Au NPs content and shown a highest H_2 evolution rate of $29.21 \mu\text{mol.h}^{-1}$ for CN-7Au photocatalyst sample. Further increase in Au content beyond 7 ml, the H_2 evolution rate was decreased. Therefore Au NPs played a significant role in enhancing the H_2 evolution rates of photocatalyst samples via surface plasmon resonance effect. The stability of optimized photocatalysts sample CN-7Au was determined by performing the time-cycles and the results were given in Fig. 8b. Each cycle was conducted for 4 h and after four cycles a slight decrement was observed. These results confirm that the CN-7Au photocatalysts sample was relatively stable during the photocatalytic H_2 evolution reactions. Next, the visible

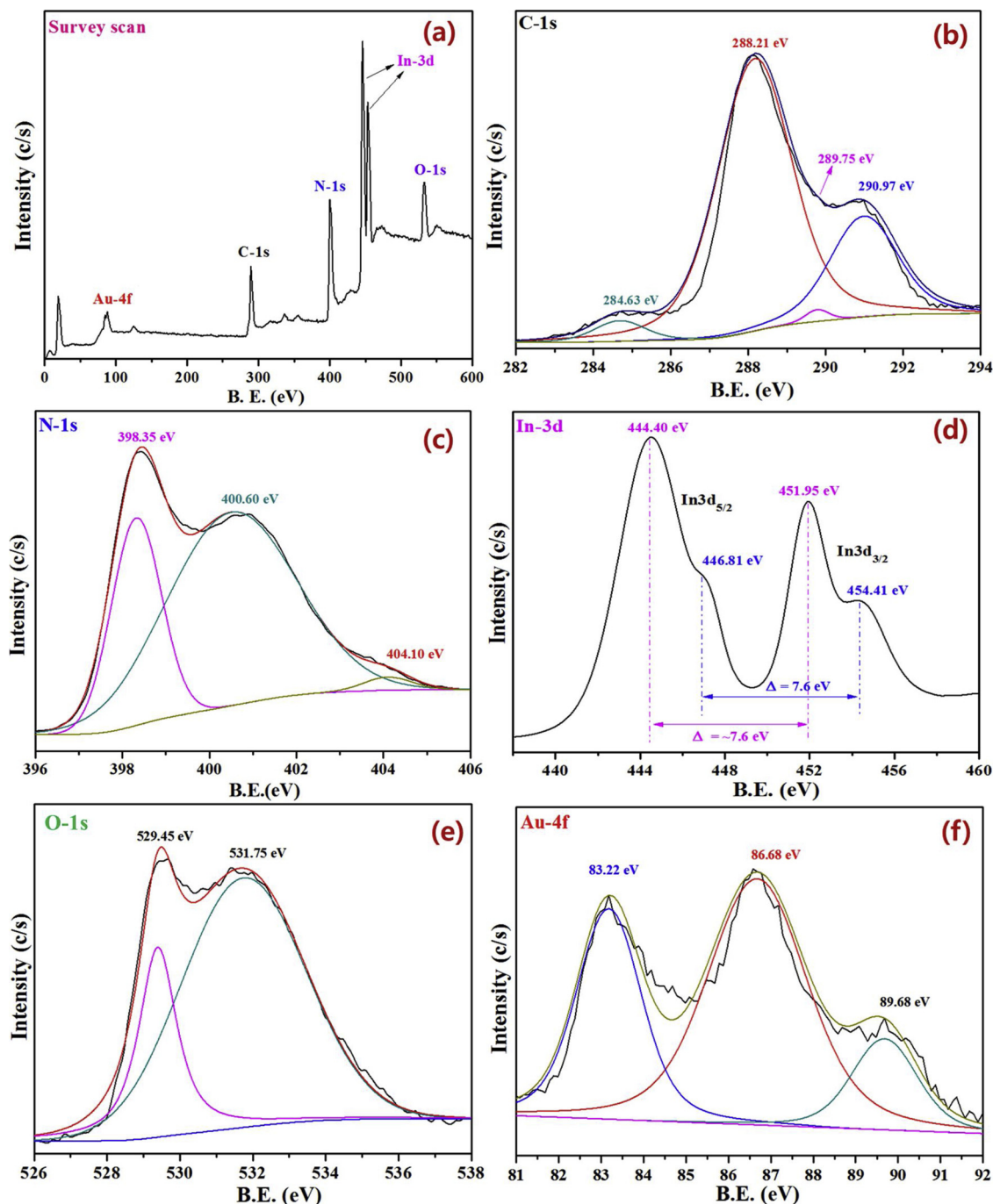


Fig. 5. XPS spectra of CN-7Au-IO sample, showing the survey spectrum (a), and high resolution XPS spectra of (b) C-1 s, (c) N-1 s, (d) In-3d, (e) O-1 s, and (f) Au-4f elements.

photocatalytic H_2 evolution rate of CN-Au nanostructures was further improved by loading In_2O_3 nanospheres and their corresponding visible photocatalytic H_2 evolution rates were shown in Fig. 8c. As expected the CN-7Au-IO photocatalyst sample shows the highest photocatalytic H_2 evolution rate of $56.48 \mu\text{mol.h}^{-1}$ which is higher than that of CN-IO ($29.52 \mu\text{mol.h}^{-1}$), CN-5Au-IO ($35.75 \mu\text{mol.h}^{-1}$) and CN-10Au-IO ($45.25 \mu\text{mol.h}^{-1}$) samples. Interestingly, the photocatalytic activity of CN nanosheets was evidently increased after loading Au NPs and then modifying with In_2O_3 nanospheres. This remarkable H_2 evolution activity of CN-7Au-IO is due to the SPR effect of Au NPs and effective charge separation between CN and IO components which will be discussed in next sections. The photostability of the CN-7Au-IO sample under identical conditions also inspected in seven consecutive runs of

28 h irradiation with fresh sacrificial reagent (10 vol% Methanol) intermittently changed in each run. As shown in Fig. 8d, a slight decrement in H_2 evolution rate was observed after four cycles for the present photocatalyst sample upon extending the photoreaction time. It is proposed that the present CN-7Au-IO nanocomposite has substantial photostability for H_2 production under visible-light irradiation. Several researchers confirmed that the introduction of other semiconductors onto $g-C_3N_4$ can significantly improve the photocatalytic performance in which the CB potential difference allows the photogenerated electrons to transfer more easily via the heterojunctions [72–74] and then enhanced photocatalytic activity will be observed. For hydrogen evolution reaction, the optimized CN-7Au-IO photocatalyst system exhibits a quantum efficiency up to 2.5% ($\lambda = 420 \text{ nm}$). Table 2 enlists the H_2

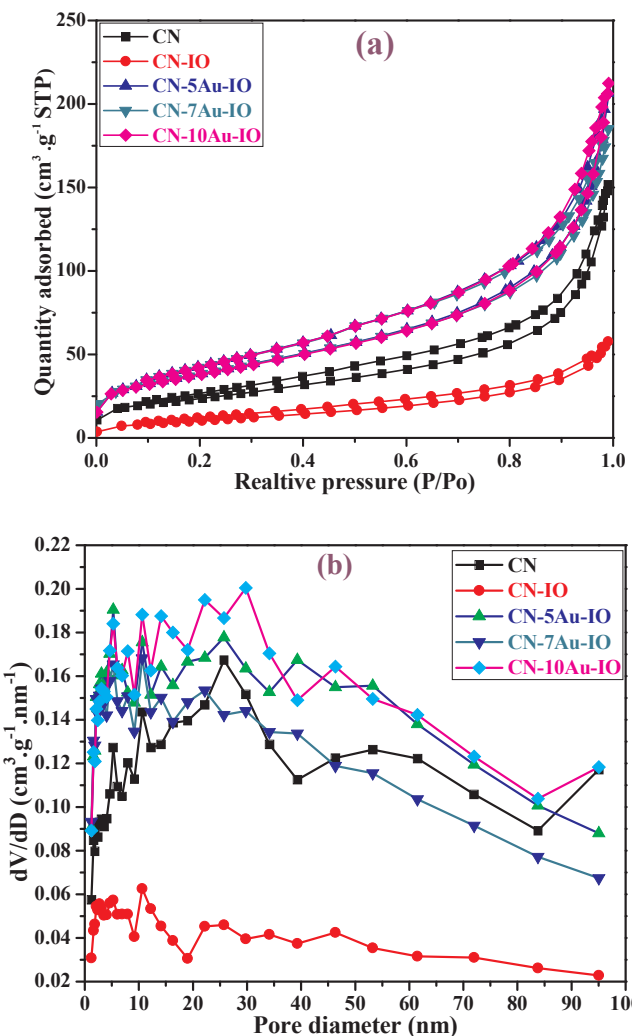


Fig. 6. (a) N₂ adsorption-desorption isotherms, and (b) pore-size distribution curves of CN, CN-IO, CN-5Au-IO, CN-7Au-IO, and CN-10Au-IO photocatalyst samples.

Table 1
BET surface area and pore structure parameters of CN and CN-Au-IO samples.

Samples	S _{BET} (m ² /g)	Mean pore diameter (nm)	Pore volume (cm ³ /g)
CN	84.87	10.93	0.23
CN-IO	38.18	9.32	0.09
CN-5Au-IO	138.26	9.05	0.31
CN-7Au-IO	137.4	8.27	0.28
CN-10Au-IO	136.28	9.47	0.32

evolution rates and quantum yields of g-C₃N₄ based heterostructures and the results obtained in the present work are higher and also comparable to the previous reports.

To provide the evidence in the improved photocatalytic H₂ evolution reaction, photocurrent responses of pure CN, CN-IO and CN-7Au-IO photocatalyst samples were taken under visible light irradiation. Generally, the higher photocurrent designates the more efficient charge carrier's separation and transfer. Fig. 9a shows the photocurrent density vs time curves of CN, CN-IO and CN-7Au-IO samples at a bias potential of 0.5 V. As seen from Fig. 9a, the photocurrent value of the CN-7Au-IO is higher than CN and CN-IO samples. This behavior may be caused by a ternary nanocomposite structure consisting of Au and In₂O₃ NPs and more effective in separation of photoinduced electron-hole pairs than the remaining samples. In other words, the higher photocarrier

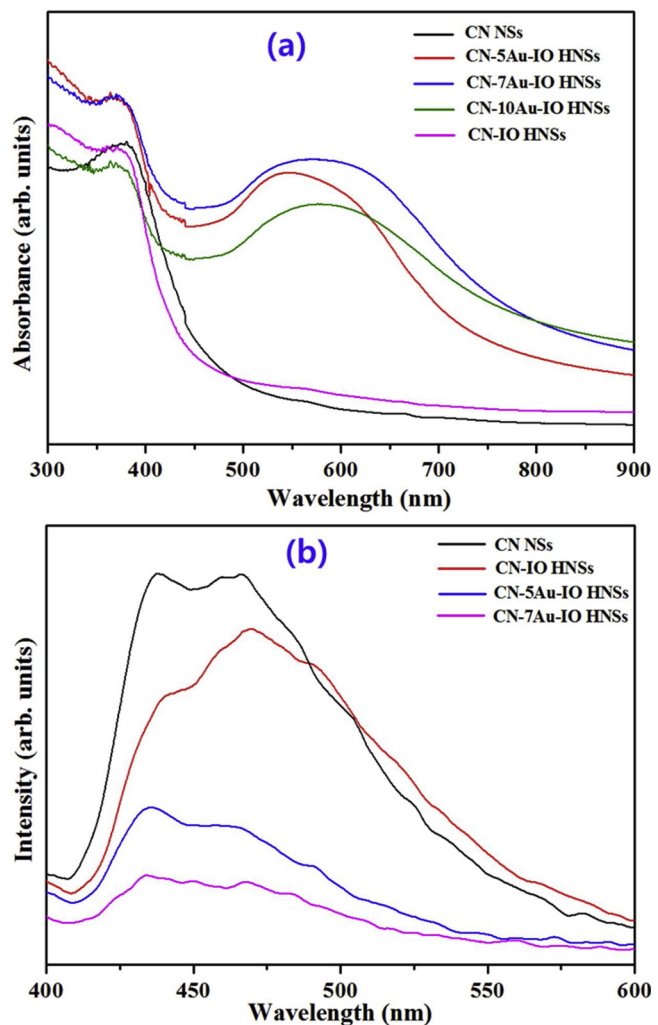


Fig. 7. (a) UV-vis diffuse reflectance and (b) Photoluminescence spectra of CN and CN-IO and CN-Au-IO photocatalyst samples.

separation efficiency in CN-7Au-IO is ascribed to the decoration of Au and In₂O₃ nanospheres that can accelerated the separation of electron-hole pairs which in turn produces the higher photocatalytic H₂ evolution activity. Next, the EIS spectral analysis was utilized to further assess the charge transfer property. Fig. 9b shows the EIS of CN, CN-IO and CN-7Au-IO. The EIS results given in Fig. 9b show that the CN-7Au-IO sample exhibited the lowest resistance for charge transfer, which helps the greater charge separation of charged carriers. The EIS-Nyquist plot is fitted to the Randle's equivalent circuit (Fig. 10b inset), in which R_{ct} is charge transfer resistance, R_s is solution resistance and C is interface capacitance. From the fitted data, EIS parameters are given in Table 3. From Fig. 9b and Table 3, it is verified that the highest arc of pure CN sample is accompanied with higher charge transfer resistance, and CN-IO hybrid system shown decreased arc radius after loading with In₂O₃ nanospheres, suggesting the improvement of charged carrier's separation efficiency from heterojunctions between g-C₃N₄ and In₂O₃. Among the samples, CN-7Au-IO photocatalyst displays the lowest charge transfer resistance confirming the higher charge separation/transfer efficiency owing to the optimal hybrid heterojunction interfaces. This suggests that the proposed heterostructure can allow the effective charge transfer and reduce the interfacial resistance to realize the better performance in photocatalytic reactions.

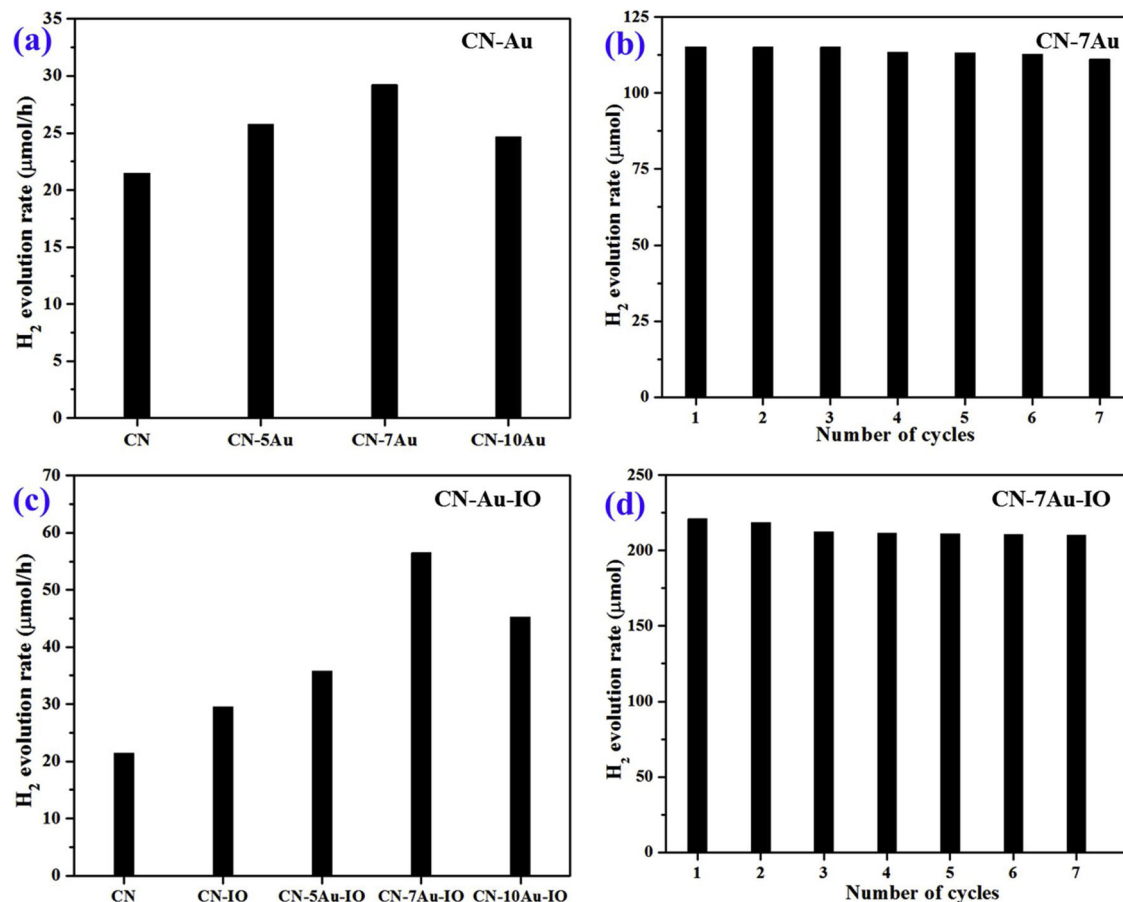


Fig. 8. (a) Photocatalytic H₂ evolution rates of CN, CN-Au nanostructures, (b) Stability tests for CN-7Au sample, (c) Photocatalytic H₂ evolution rates of CN-Au-IO samples, (d) Stability tests for CN-7Au-IO sample.

Table 2

Comparison between the H₂ evolution rate and quantum efficiency values of reported g-C₃N₄ based photocatalysts.

Catalyst	Light source ($\lambda > 420$ nm)	H ₂ evolution rate ($\mu\text{mol} \cdot \text{g}^{-1} \cdot \text{h}^{-1}$)	Quantum Efficiency	Ref.
g-C ₃ N ₄ -TiO ₂	300 W Xe lamp	18200	0.57%	[41]
g-C ₃ N ₄ -Fe ₂ O ₃	300 W Xe lamp	31400	44.35%	[42]
g-C ₃ N ₄ -Cu ₃ P	300 W Xe lamp	159.41	–	[44]
g-C ₃ N ₄ -Ni ₃ C	350 W Xe lamp	15.18	0.40%	[45]
g-C ₃ N ₄ -CoP	300 W Xe lamp	67.2	0.12%	[48]
g-C ₃ N ₄ -CuS	300 W Xe lamp	348	–	[49]
g-C ₃ N ₄ -NiS	300 W Xe lamp	366.4	–	[50]
g-C ₃ N ₄ -Au-TiO ₂	300 W Xe lamp	350	0.18%	[53]
g-C ₃ N ₄ -MnO _x -Au-TiO ₂	300 W Xe lamp	313	2.78%	[54]
g-C ₃ N ₄ -Au-SnO ₂	300 W Xe lamp	770	–	[55]
g-C ₃ N ₄ -NiS	300 W Xe lamp	515	–	[60]
g-C ₃ N ₄ -Ni ₃ B/Ni(OH) ₂	300 W Xe lamp	352.43	0.70%	[64]
g-C ₃ N ₄ -SiO ₂ -TiO ₂	300 W Xe lamp	572.6	–	[74]
g-C ₃ N ₄ -Au-In ₂ O ₃	150 W Xe lamp	5648	2.50%	This work

3.5. Photocatalytic H₂ evolution mechanism

To determine the effect of heterostructure on the photocatalytic activity, initially the energy bandstructure of both semiconductors g-C₃N₄ and In₂O₃ was investigated. The band edge (CB and VB) positions of both materials can be estimated by the following formula [75,76],

$$E_{\text{CB}} = \chi - E^{\text{e}} - \frac{1}{2} E_{\text{g}} \quad (2)$$

$$E_{\text{VB}} = E_{\text{CB}} + E_{\text{g}} \quad (3)$$

Where E_{VB} is the VB edge potential, E_{CB} is the CB edge potential, and χ is the electronegativity. E_g is the band gap of the semiconductor and E_e is the energy of free electrons on the hydrogen scale ≈ 4.5 eV. From

UV-vis spectra, the E_g values of g-C₃N₄ and In₂O₃ can be estimated as 2.83 and 2.80 eV respectively. The VB edge positions are calculated from XPS VB spectra as 1.83 and 2.2 eV for g-C₃N₄ and In₂O₃ respectively. From the above data, CB positions of g-C₃N₄ and In₂O₃ are approximately calculated as -1.0 and -0.6 eV respectively. Both band sets of In₂O₃ are relatively lower than of g-C₃N₄ (Fig. S5). These band structures determined from both UV-vis and XPS valence band spectra clearly forms heterojunctions between both studied semiconductors.

According to the above discussions, the proposed mechanism for charge carriers generation, separation and the possible reactions during the visible light irradiation is given in Fig. 10. We consider that the improved photocatalytic H₂ evolution activities from CN-7Au-IO by

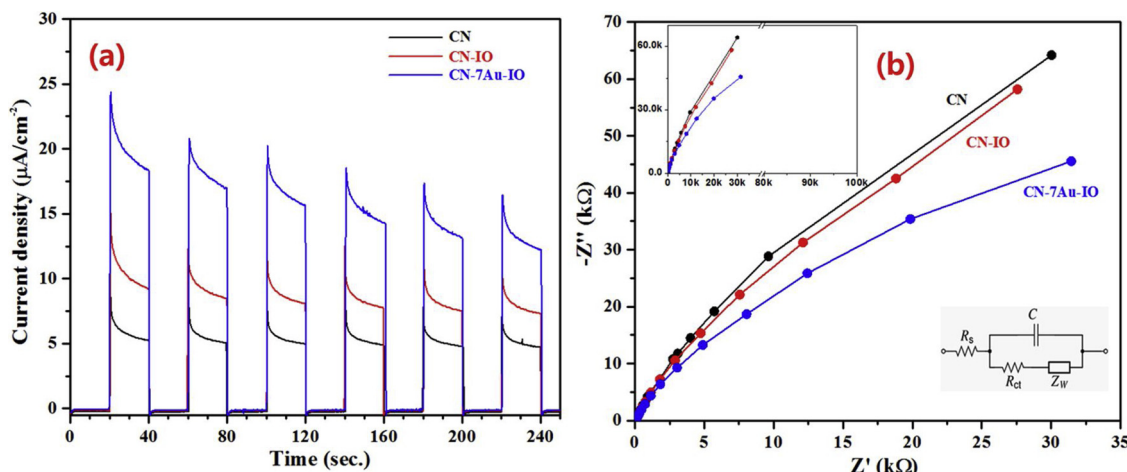


Fig. 9. Transient photocurrent responses (a) and electrochemical impedance spectra (b) of CN, CN-IO, and CN-7Au-IO heterostructures.

decorating Au and In_2O_3 nanocomponents are due to the effective charge transfer at the heterojunctions formed between $\text{g-C}_3\text{N}_4$, Au and In_2O_3 components. Based on $\text{g-C}_3\text{N}_4$ and In_2O_3 energy band levels, and coupling of Au NPs in a final CN-7Au-IO sample, different possible charge transfer processes will be occurred and are shown in Fig. 10. The VB and CB edge potentials of $\text{g-C}_3\text{N}_4$ are at + 1.83 eV and -1.0 eV, whereas for In_2O_3 are + 2.2 eV and -0.6 eV, respectively. The heterojunctions formed between CN and In_2O_3 , under visible light radiation, the electrons in the valence bands of CN are excited to conduction band of CN and immediately transferred to CB of In_2O_3 , greatly suppressing the recombination between electrons and holes. These collected electrons, together with the photoexcited electrons of In_2O_3 , are capable of reducing H^+ into H_2 . For CN-7Au-IO composite, Au NPs can act as an electron transportation bridge to increase the efficient charge separation in $\text{g-C}_3\text{N}_4$ [52]. Moreover, the deposited Au NPs can effectively improve the visible light absorption via SPR effect. In the cases of CN-Au and/or In_2O_3 -Au metal semiconductor heterostructures, it is believed that the photogenerated electrons of CN and IO under visible light could transfer to Au NPs as an electron sink, leading to the improved charge separation and improved visible-light activity [21,56]. It is also considerable that the contribution of Au NPs acting as a co-catalyst confirmed by recent studies that, the presence of metal NPs promotes the reverse spillover of H_2 atoms, i.e., their movement from the CN/IO material to the Au NPs. Hence it is claimed that the role of Au NPs in the improved photocatalytic H_2 evolution performance is also

Table 3
The EIS fitted parameters for the studied photocatalyst samples.

Sample	R_s (Ohm)	R_{ct} (Ohm)
CN	106.6	4305.1
CN-IO	91.25	3847.25
CN-7Au-IO	85.65	2684.21

a co-catalytic besides SPR effect and would assist in the improvement of diffusion/migration of H_2 atoms [77–79]. Thus, it is established that the formed CN-7Au-IO platform is much favourable to increase the charge separation from plasmonic Au and heterostructures with In_2O_3 components for efficient H_2 evolution under visible-light irradiation.

3.6. Studies on morphological, geometrical and chemical states of Au NPs

To well understand the role of Au NPs for enhanced visible light H_2 evolution activity, we have further carried out the structural and morphological characterizations for all samples containing Au NPs. Fig. S6 depicts the HR-TEM images of CN-Au and CN-Au-IO samples, in which the Au NPs were uniformly distributed on the surface of CN nanosheets. To understand the Au particle size distribution over the different photocatalyst samples, high resolution STEM images of CN-Au and CN-Au-IO samples were also recorded and their corresponding particle distribution plots were given in Fig. 11. As seen from

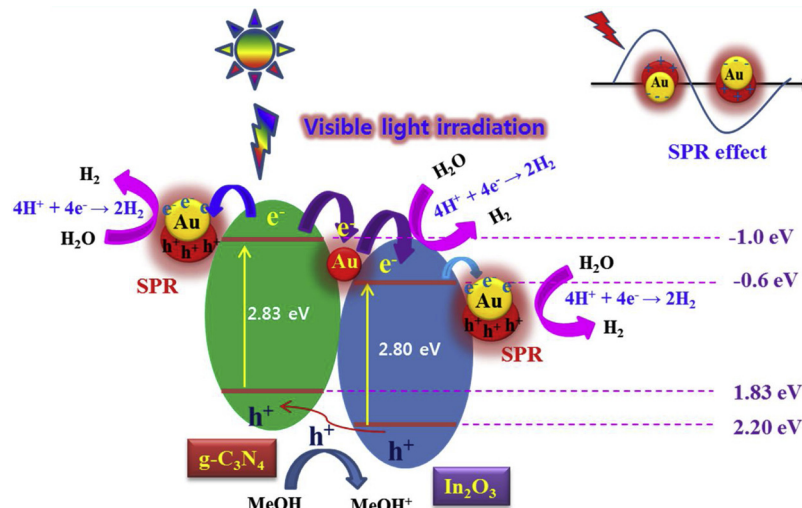


Fig. 10. Schematic illustration of charge carriers' migration/separation in CN-7Au-IO photocatalyst sample.

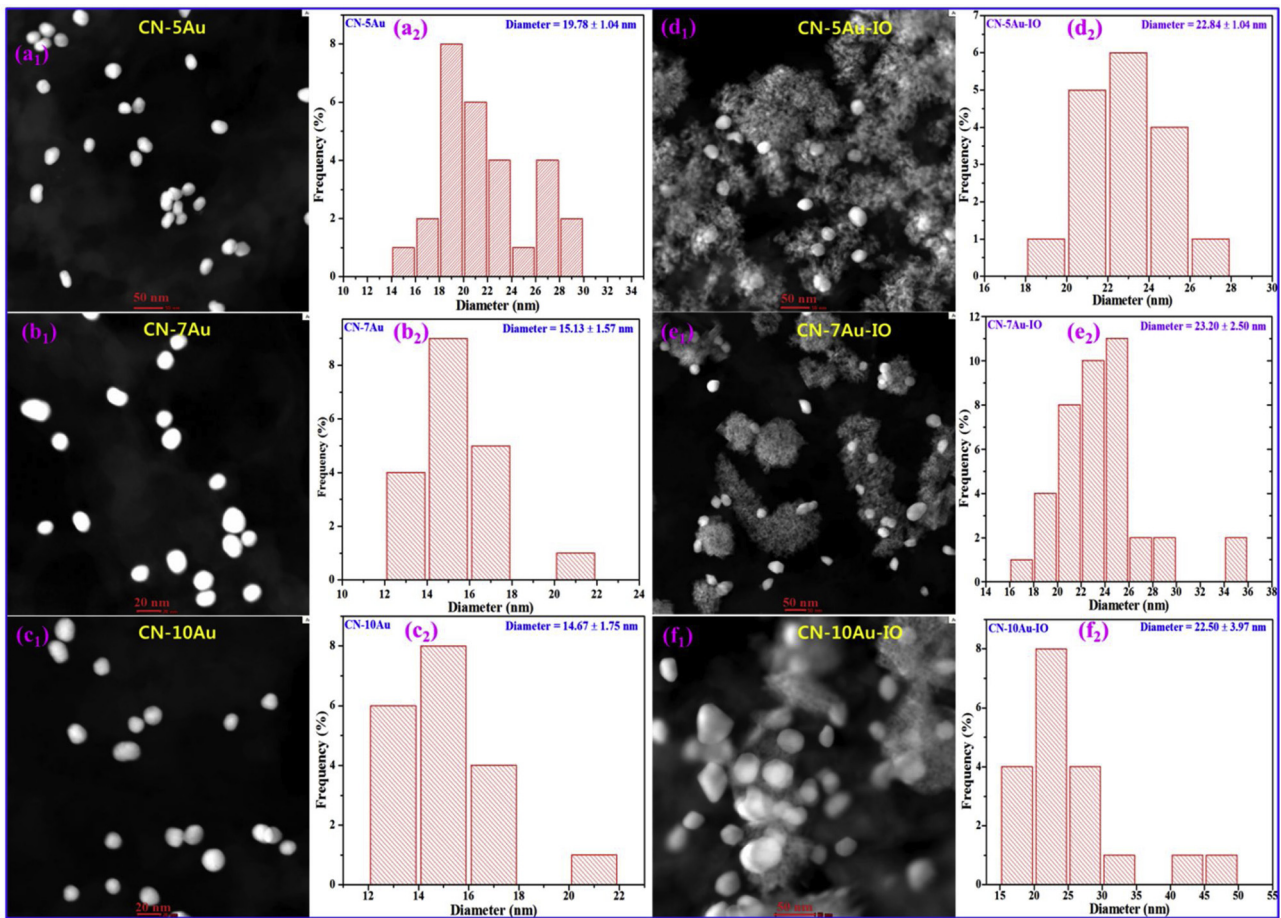


Fig. 11. High resolution STEM images and particle size distribution profiles of CN-Au and CN-Au-IO samples.

Fig. 11a₁,b₁,c₁, Au NPs were successfully anchored on the surface of CN nanosheets and their particle size distributions (Fig. 11a₂,b₂,c₂) were measured as about 20, 15, and 14 nm for CN-5Au, CN-7Au, and CN-10Au respectively. Hydrothermal reaction between CN and Au NPs results a slight changes in the particle sizes of Au NPs and the optimized CN-7Au exhibit the higher photocatalytic H₂ evolution rate. Next, Fig. 11d₁,e₁,f₁ represents the STEM images of CN-5Au-IO, CN-7Au-IO and CN-10Au-IO samples in which the bright Au NPs with In₂O₃ nanospheres were distributed on the surface of CN nanosheets. We further analyzed the nanoparticle size distributions from these STEM images and displayed in Fig. 11d₂,e₂,f₂. Size distribution analysis of Au NPs revealed that an average particle size of 23 nm which is higher than the freshly prepared Au NPs. In addition to this it is also observed that the geometrical shapes of Au NPs observed from STEM images are significantly differ from each other and shape of Au NPs evolved from spherical to irregular shaped NPs. Hydrothermal reaction and then subsequent calcination processes caused the increment in Au NPs size and shape in all samples.

The CN-Au-IO photocatalysts samples prepared by a hydrothermal growth and subsequent calcination route, using different amounts of Au content were also analyzed by high resolution XPS spectra by recording the Au-4f core levels. Avantage program was used for the deconvolution of Au-4f core-level spectra and background type was Shirley. Fig. 12 shows the Au-4f spectra of CN-5Au-IO, CN-7Au-IO, and CN-10Au-IO samples. As seen from Fig. 12, all the samples are characterized by three BE peaks at 83.60, 86.55, and 89.69 eV for CN-5Au-IO, 83.22, 86.68, and 89.72 eV for CN-7Au-IO and 83.74, 87.10, and 89.95 for CN-10Au-IO. The first two peaks assigned to spin-orbit coupling of Au-4f_{7/2} and Au-4f_{5/2} core-levels of Au metallic state (Au⁰) and the last peak is attributed to the oxidized Au state, Au³⁺. In the current work, the

observed BE values, for example Au-4f_{7/2} (83.60, 83.22, and 83.74 for three samples) are lower than the bulk Au-4f_{7/2} (84.0 eV). This negative shift is due to the variations in electronic properties as a function of geometrical or particle size, electron transfer from CN nanosheets or In₂O₃ nanospheres to the Au metal NPs and similar observations were also found in the literatures [69,80,81]. The sample, CN-7Au-IO exhibited a more negative shift which arises due to the transfer of more electrons from CN and In₂O₃ to Au NPs and also specifies that the charge densities increase in metal Au NPs as a results of electronic redistribution via heterojunctions, then the obtained heterostructure system can cause in the increase of photocatalytic H₂ evolution activity than the remaining samples. The peaks observed at 89.69, 89.72, and 89.95 for CN-5Au-IO, CN-7Au-IO, and CN-10Au-IO respectively were originated from the partial oxidation of Au NPs during the calcination process [82,83].

4. Conclusions

In summary, a polymeric g-C₃N₄ with a bandgap of 2.83 eV was prepared by a simple pyrolysis process, and then the g-C₃N₄-Au-In₂O₃ heterostructured ternary nanocomposite was prepared via a facile hydrothermal method followed by a calcination process. The structural properties of the prepared samples were studied by XRD, XPS, UV-vis absorption and PL spectra, suggesting that the Au NPs and In₂O₃ nanospheres were loaded on the surface of g-C₃N₄ nanosheets surface. From the results of HRTEM images, Au and In₂O₃ components successfully formed heterojunctions with each other on CN nanosheets. Also, this facile and easy incorporation of Au and In₂O₃ significantly promotes the interface free carriers separation, shortens the migration resistance of CN-Au-IO photocatalyst, and accelerates the H₂ evolution

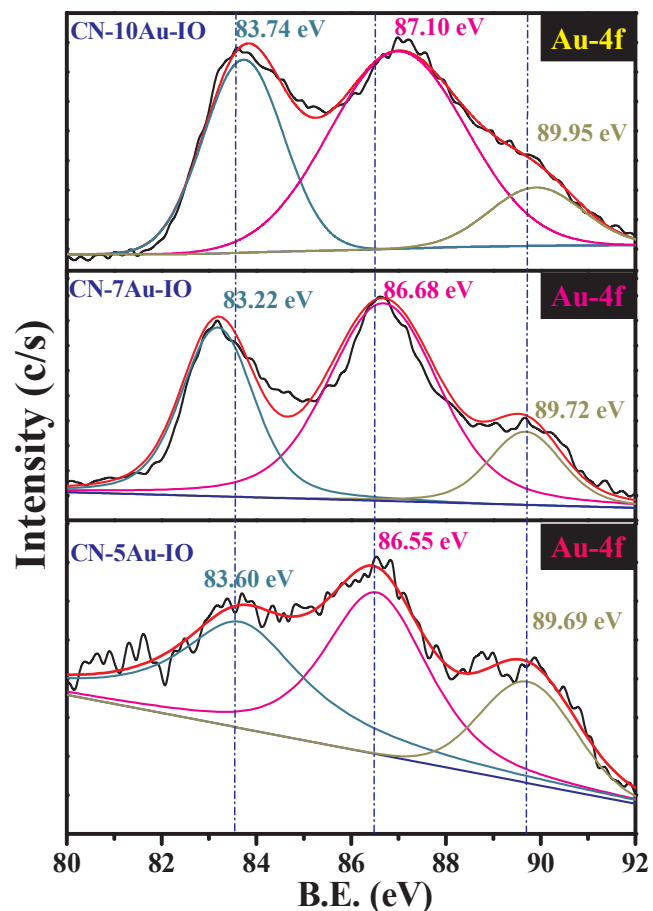


Fig. 12. Comparison of Au-4f core-level spectra in all CN-Au-IO photocatalyst samples.

reaction rate according to the PL and EIS results. The prepared CN-Au-IO heterostructured photocatalyst samples are highly active for H_2 evolution reactions under the visible light irradiation; and Au content significantly affects the photocatalytic activity. CN-Au-IO photocatalyst samples shows the highest H_2 evolution rate, more specifically the optimized sample CN-7Au-IO exhibited the highest H_2 evolution rate of $56.48 \mu\text{mol.h}^{-1}$ which is higher than CN ($21.45 \mu\text{mol.h}^{-1}$) and CN-IO ($29.52 \mu\text{mol.h}^{-1}$) samples. The SPR effect from Au NPs and heterojunctions formed between three components resulted the improved visible light harvesting and suppressed the electron-hole recombination, thereby promoting the higher photocatalytic activity in CN-7Au-IO system. The current work shows that the charge migration/separation route in a ternary composite system provides a model for designing and comprehensive understanding of $\text{g-C}_3\text{N}_4$ -metal-metal oxide semiconductor system for efficient solar to chemical energy applications.

Acknowledgments

This work was supported by the National Research Foundation (NRF) of Korea grant funded by the Korea government (MSIT) (No: 2018R1A2B6004746), for which authors are very grateful.

Appendix A. Supplementary data

Supplementary material related to this article can be found, in the online version, at doi:<https://doi.org/10.1016/j.apcatb.2019.01.075>.

References

- [1] A. Fujishima, K. Honda, Electrochemical photolysis of water at a semiconductor electrode, *Nature* 238 (1972) 37–38.
- [2] K. Akihiko, M. Yugo, Heterogeneous photocatalyst materials for water splitting, *Chem. Soc. Rev.* 38 (2009) 253–278.
- [3] F.E. Osterloh, Inorganic materials as catalysts for photochemical splitting of water, *Chem. Mater.* 20 (2008) 35–54.
- [4] X. Chen, S. Shen, L. Guo, S. Mao, Semiconductor-based photocatalytic hydrogen generation, *Chem. Rev.* 110 (2010) 6503–6570.
- [5] S.Y. Tee, K.Y. Win, W.S. Teo, L.D. Koh, S. Liu, C.P. Teng, M.Y. Han, Recent progress in energy-driven water splitting, *Adv. Sci.* 4 (2017) 1600337.
- [6] X.C. Wang, K. Maeda, A. Thomas, K. Takanabe, G. Xin, J.M. Carlsson, K. Domen, M. Antonietti, A metal-free polymeric photocatalyst for hydrogen production from water under visible light, *Nat. Mater.* 8 (2009) 76–80.
- [7] J. Zhang, M. Grzelczak, Y.D. Hou, K. Maeda, K. Domen, X.Z. Fu, M. Antonietti, X.C. Wang, Photocatalytic oxidation of water by polymeric carbon nitride nano-hybrids made of sustainable elements, *Chem. Sci.* 3 (2012) 443–446.
- [8] G. Zhang, M. Zhang, X. Ye, X. Qiu, S. Lin, X. Wang, Iodine modified carbon nitride semiconductors with visible light photocatalysts for hydrogen evolution, *Adv. Mater.* 26 (2014) 805–809.
- [9] L. Li, J. Yan, T. Wang, Z.J. Zhao, J. Zhang, J. Gong, N. Guan, Sub-10 nm rutile titanium dioxide nanoparticles for efficient visible-light-driven photocatalytic hydrogen production, *Nat. Commun.* 6 (2015) 5881.
- [10] K. Maeda, K. Teramura, D. Lu, T. Takata, N. Saito, Y. Inoue, K. Domen, Photocatalyst releasing hydrogen from water, *Nature* 440 (2006) 295.
- [11] Z.G. Zou, J.H. Ye, K. Sayama, H. Arakawa, Direct splitting of water under visible light irradiation with an oxide semiconductor photocatalyst, *Nature* 414 (2001) 625–627.
- [12] I. Tsuji, H. Kato, A. Kudo, Visible-light-induced H_2 evolution from an aqueous solution containing sulfide and sulfite over a $\text{ZnS}-\text{CuInS}_2-\text{AgInS}_2$ solid-solution photocatalyst, *Angew. Chem. Int. Ed.* 44 (2005) 3565–3568.
- [13] R.K. Chava, J.Y. Do, M. Kang, Smart hybridization of Au coupled CdS nanorods with few layered MoS_2 nanosheets for high performance photocatalytic hydrogen evolution reaction, *ACS Sustain. Chem. Eng.* 6 (2018) 6445–6447.
- [14] X. Wang, K. Maeda, X. Chen, K. Takanabe, K. Domen, Y. Hou, X. Fu, M. Antonietti, Polymer semiconductors for artificial photosynthesis: hydrogen evolution by mesoporous graphitic carbon nitride with visible light, *J. Am. Chem. Soc.* 131 (2009) 1680–1681.
- [15] K. Maeda, X. Wang, Y. Nishihara, D. Lu, M. Antonietti, K. Domen, Photocatalytic activities of graphitic carbon nitride powder for water reduction and oxidation under visible light, *J. Phys. Chem. C* 113 (2009) 4940–4947.
- [16] S. Yang, Y. Gong, J. Zhang, L. Zhan, L. Ma, Z. Fang, R. Vajtai, X. Wang, P.M. Ajayan, Exfoliated graphitic carbon nitride nanosheets as efficient catalysts for hydrogen evolution under visible light, *Adv. Mater.* 25 (2013) 2452–2456.
- [17] S. Cao, J. Low, J. Yu, M. Jaroniec, Polymeric photocatalysts based on graphitic carbon nitride, *Adv. Mater.* 27 (2015) 2150–2176.
- [18] J. Zhang, Y. Chen, X. Wang, Two-dimensional covalent carbon nitride nanosheets: synthesis, functionalization, and applications, *Energy Environ. Sci.* 8 (2015) 3092–3108.
- [19] W.-J. Ong, L.-L. Tan, Y.H. Ng, S.-T. Yong, S.-P. Chai, Graphitic carbon nitride ($\text{g-C}_3\text{N}_4$) based photocatalysts for artificial photosynthesis and environmental remediation: are we a step closer to achieving sustainability? *Chem. Rev.* 116 (2016) 7159–7329.
- [20] S. Samanta, S. Martha, K. Parida, Facile synthesis of $\text{Au/g-C}_3\text{N}_4$ nanocomposites: an inorganic/organic hybrid plasmonic photocatalyst with enhanced hydrogen gas evolution under visible-light irradiation, *ChemCatChem* 6 (2014) 1453–1462.
- [21] L. Wang, C.Y. Wang, X. Hu, H. Xue, H. Pang, Metal/graphitic carbon nitride composites: synthesis, structures, and applications, *Chem. Asian J.* 11 (2016) 3305–3328.
- [22] Y.J. Zhang, T. Mori, J.H. Ye, M. Antonietti, Phosphorus-doped carbon nitride solid: enhanced electrical conductivity and photocurrent generation, *J. Am. Chem. Soc.* 132 (2010) 6294–6295.
- [23] L.-F. Gao, T. Wen, J.-T. Xu, X.-P. Zhai, M. Zhao, G.-W. Hu, P. Chen, Q. Wang, H. Zhang, Iron-doped carbon nitride-type polymers as homogeneous organocatalysts for visible light-driven hydrogen evolution, *ACS Appl. Mater. Interfaces* 8 (2016) 617–624.
- [24] X.C. Wang, X.F. Chen, A. Thomas, X.Z. Fu, M. Antonietti, Metal-containing carbon nitride compounds: a new functional organic–metal hybrid material, *Adv. Mater.* 21 (2009) 1609–1612.
- [25] G. Liu, P. Niu, C.H. Sun, S.C. Smith, Z.G. Chen, G.Q. Lu, H.-M. Cheng, Unique electronic structure induced high photoreactivity of sulfur-doped graphitic C_3N_4 , *J. Am. Chem. Soc.* 132 (2010) 11642–11648.
- [26] X.F. Chen, J.S. Zhang, X.Z. Fu, M. Antonietti, X.C. Wang, Fe- $\text{g-C}_3\text{N}_4$ -Catalyzed oxidation of benzene to phenol using hydrogen peroxide and visible light, *J. Am. Chem. Soc.* 131 (2009) 11658–11659.
- [27] Q. Gu, Y. Liao, L. Yin, J. Long, X. Wang, C. Xue, Template-free synthesis of porous graphitic carbon nitride microspheres for enhanced photocatalytic hydrogen generation with high stability, *Appl. Catal. B* 165 (2015) 503–510.
- [28] S. Zhao, Y.W. Zhang, J.S. Fang, H. Zhang, Y.Y. Wang, Y.M. Zhou, W.X. Chen, C. Zhang, Self-assembled mesoporous carbon nitride with tunable texture for enhanced visible-light photocatalytic hydrogen evolution, *ACS Sustain. Chem. Eng.* 6 (2018) 8291–8299.
- [29] Y.J. Cui, Z.X. Ding, X.Z. Fu, X.C. Wang, Construction of conjugated carbon nitride nanoarchitectures in solution at low temperatures for photoredox catalysis, *Angew.*

Chem. Int. Ed. 51 (2012) 11814–11818.

[30] Y. Kofuji, Y. Isobe, Y. Shiraishi, H. Sakamoto, S. Tanaka, S. Ichikawa, T. Hirai, Carbon nitride–aromatic diimide–graphene nanohybrids: metal-free photocatalysts for solar-to-hydrogen peroxide energy conversion with 0.2% efficiency, *J. Am. Chem. Soc.* 138 (2016) 10019–10025.

[31] E.S.D. Silva, N.M.M. Moura, M.G.P.M.S. Neves, A. Coutinho, M. Prieto, C.G. Silva, J.L. Faria, Novel hybrids of graphitic carbon nitride sensitized with free-base meso-tetrakis(carboxyphenyl) porphyrins for efficient visible light photocatalytic hydrogen production, *Appl. Catal. B* 221 (2018) 56–69.

[32] P.J. Yang, R.R. Wang, M. Zhou, X.C. Wang, Photochemical construction of carbon-nitride structures for red-light redox catalysis, *Angew. Chem. Int. Ed.* 57 (2018) 8674–8677.

[33] H.H. Ou, X.R. Chen, L.H. Lin, Y.X. Fang, X.C. Wang, Biomimetic donor–acceptor motifs in conjugated polymers for promoting exciton splitting and charge separation, *Angew. Chem. Int. Ed.* 57 (2018) 8729–8733.

[34] J.S. Zhang, G.G. Zhang, X.F. Chen, S. Lin, L. Mohlmann, G. Dolega, G. Lipner, M. Antonietti, S.F. Blechert, X.C. Wang, Co-monomer control of carbon nitride semiconductors to optimize hydrogen evolution with visible light, *Angew. Chem. Int. Ed.* 51 (2012) 3183–3187.

[35] Z.Z. Lin, X.C. Wang, Nanostructure engineering and doping of conjugated carbon nitride semiconductors for hydrogen photosynthesis, *Angew. Chem. Int. Ed.* 52 (2013) 1735–1738.

[36] P. Yang, H.H. Ou, Y.X. Fang, X.C. Wang, A facile steam reforming strategy to de-laminate layered carbon nitride semiconductors for photoredox catalysis, *Angew. Chem. Int. Ed.* 56 (2017) 3992–3996.

[37] Y. Chen, G. Jia, Y.F. Hu, G.Z. Fan, Y. Hong, H. Tsang, Z.S. Li, Z.G. Zou, Two-dimensional nanomaterials for photocatalytic CO₂ reduction to solar fuels, *Sustain. Energy Fuels* 1 (2017) 1875–1898.

[38] P. Niu, L.L. Zhang, G. Liu, H.-M. Cheng, Graphene-like carbon nitride nanosheets for improved photocatalytic activities, *Adv. Funct. Mater.* 22 (2012) 4763–4770.

[39] J.H. Sun, J.S. Zhang, M.W. Zhang, M. Antonietti, X.Z. Fu, X.C. Wang, Bioinspired hollow semiconductor nanospheres as photosynthetic nanoparticles, *Nat. Commun.* 3 (2012) 1139.

[40] D.D. Zheng, X.-N. Cao, X.C. Wang, Precise formation of a hollow carbon nitride structure with a Janus surface to promote water splitting by photoredox catalysis, *Angew. Chem. Int. Ed.* 55 (2016) 11512–11516.

[41] Wenli Gu, Feixue Lu, Chao Wang, Shigenori Kuga, Lizhu Wu, Yong Huang, Min Wu, Face-to-face interfacial assembly of ultrathin g-C₃N₄ and anatase TiO₂ nanosheets for enhanced solar photocatalytic activity, *ACS Appl. Mater. Interfaces* 9 (2017) 28674–28684.

[42] X. She, J.J. Wu, H. Xu, J. Zhong, Y. Wang, Y.H. Song, K.Q. Nie, Y. Liu, Y.C. Yang, M.-T.F. Rodrigues, R. Vajtai, J. Lou, D.L. Du, H.M. Li, P.M. Ajayan, High efficiency photocatalytic water splitting using 2D α -Fe₂O₃/g-C₃N₄ Z-Scheme catalysts, *Adv. Energy Mater.* 7 (2017) 1700025.

[43] Xuqiang Hao, Jun Zhou, Zhiwei Cui, Yicong Wang, Ying Wang, Zhigang Zou, Zn-vacancy mediated electron-hole separation in ZnS/g-C₃N₄ heterojunction for efficient visible-light photocatalytic hydrogen production, *Appl. Catal. B* 229 (2018) 41–51.

[44] Rongchen Shen, Jun Xie, Xinyong Lu, Xiaobo Chen, Xin Li, Bifunctional Cu₃P decorated g-C₃N₄ nanosheets as a highly active and robust visible-light photocatalyst for H₂ production, *ACS Sustain. Chem. Eng.* 6 (2018) 4026–4036.

[45] Kelin He, Jun Xie, Zhao-Qing Liu, Neng Li, Xiaobo Chen, Jun Hu, Xin Li, Multi-functional Ni₃C cocatalyst/g-C₃N₄ nanoheterojunctions for robust photocatalytic H₂ evolution under visible light, *J. Mater. Chem. A* 6 (2018) 13110–13122.

[46] Erbing Hua, Gang Liu, Guan Zhang, Xiaoxiang Xu, In situ fabrication of two-dimensional g-C₃N₄/Ba_{0.5}Ta_{0.5}O₁₅ nanosheet heterostructures with efficient charge separations and photocatalytic hydrogen evolution under visible light illumination, *Dalton Trans.* 47 (2018) 4360–4367.

[47] H.F. Shi, G.Q. Chen, C.L. Zhang, Z.G. Zou, Polymeric g-C₃N₄ coupled with NaNbO₃ nanowires toward enhanced photocatalytic reduction of CO₂ into renewable fuel, *ACS Catal.* 4 (2014) 3637–3643.

[48] X.-J. Sun, D.-D. Yang, H. Dong, X.-B. Meng, J.-L. Sheng, X. Zhang, J.-Z. Wei, F.-M. Zhang, ZIF-derived CoP as a cocatalyst for enhanced photocatalytic H₂ production activity of g-C₃N₄, *Sustain. Energy Fuels* 2 (2018) 1356–1361.

[49] Rongchen Shen, Jun Xie, Pinyu Guo, Leshi Chen, Xiaobo Chen, Xin Li, Bridging the g-C₃N₄ nanosheets and robust CuS cocatalysts by metallic acetylene black interface mediators for active and durable photocatalytic H₂ production, *ACS Appl. Energy Mater.* 1 (2018) 2232–2241.

[50] Jiuqing Wen, Jun Xie, Zhuohong Yang, Rongchen Shen, Huiyi Li, Xing Yi Luo, Xiaobo Chen, Xin Li, Fabricating the robust g-C₃N₄ nanosheets/carbon/NiS multiple heterojunctions for enhanced photocatalytic H₂ generation: an insight into the trifunctional roles of nanocarbons, *ACS Sustain. Chem. Eng.* 5 (2017) 2224–2236.

[51] Li Shi, Zhao Lib Kyle Marcus, Guanzhi Wang, Kun Liang, Wenhan Niu, Yang Yang, Integration of Au nanoparticles with a g-C₃N₄ based heterostructure: switching charge transfer from type-II to Z-scheme for enhanced visible light photocatalysis, *Chem. Commun.* 54 (2018) 3747–3750.

[52] J. Zhu, P. Xiao, H. Li, S.N.A. Carabineiro, Graphitic carbon nitride: synthesis, properties, and applications in catalysis, *ACS Appl. Mater. Interfaces* 6 (2014) 16449–16465.

[53] Clément Marchal, Thomas Cottineau, María Guadalupe Méndez-Medrano, Christophe Colbeau-Justin, Valérie Caps, Valérie Keller, Au/TiO₂–g-C₃N₄ nanocomposites for enhanced photocatalytic H₂ production from water under visible light irradiation with very low quantities of sacrificial agents, *Adv. Energy Mater.* 8 (2018) 1702142.

[54] Fazal Raziq, Liqun Sun, Yuying Wang, Xuliang Zhang, Muhammad Humayun, Sharafat Ali, Linlu Bai, Yang Qu, Haitao Yu, Liqiang Jing, Synthesis of large surface-area g-C₃N₄ comodified with MnO_x and Au-TiO₂ as efficient visible-light photocatalysts for fuel production, *Adv. Energy Mater.* 8 (2018) 1701580.

[55] Amir Zada, Muhammad Humayun, Fazal Raziq, Xuliang Zhang, Yang Qu, Linlu Bai, Chuanli Qin, Liqiang Jing, Honggang Fu, Exceptional visible-light-driven cocatalyst-free photocatalytic activity of g-C₃N₄ by well designed nanocomposites with plasmonic Au and SnO₂, *Adv. Energy Mater.* 6 (2016) 1601190.

[56] Xiuli Lu, Kun Xu, Pengzuo Chen, Kaicheng Jia, Liu Si, Changzheng Wu, Facile one step method realizing scalable production of g-C₃N₄ nanosheets and study of their photocatalytic H₂ evolution activity, *J. Mater. Chem. A* 2 (2014) 18924–18928.

[57] R.K. Chava, S.-Y. Oh, Y.-T. Yu, Enhanced H₂ gas sensing properties of Au@In₂O₃ core–shell hybrid metal–semiconductor hetero nanostructures, *CrystEngComm* 18 (2016) 3655–3666.

[58] H.C. Lan, L.L. Li, X.Q. An, F. Liu, C.B. Chen, H.J. Liu, J.H. Qu, Microstructure of carbon nitride affecting synergistic photocatalytic activity: hydrogen bonds vs. structural defects, *Appl. Catal. B: Environ.* 204 (2017) 49–57.

[59] H.J. Yu, R. Shi, Y.X. Zhao, T. Bian, Y.F. Zhao, C. Zhou, G.I.N. Waterhouse, Li. Zhu Wu, C. Ho Tung, T.R. Zhang, Alkali-assisted synthesis of nitrogen deficient graphitic carbon nitride with tunable band structures for efficient visible-light-driven hydrogen evolution, *Adv. Mater.* 29 (2017) 1605148.

[60] J. Wen, J. Xie, H. Zhang, A. Zhang, Y. Liu, X. Chen, X. Li, Constructing multi-functional metallic Ni interface layers in the g-C₃N₄ nanosheets/amorphous NiS heterojunctions for efficient photocatalytic H₂ generation, *ACS Appl. Mater. Interfaces* 9 (2017) 14031–14042.

[61] J. Zhang, M. Zhang, G. Zhang, X. Wang, Synthesis of carbon nitride semiconductors in sulfur flux for water photoredox catalysis, *ACS Catal.* 2 (2012) 940–948.

[62] Jinshui Zhang, Mingwen Zhang, Can Yang, Xinchen Wang, Nanospherical carbon nitride frameworks with sharp edges accelerating charge collection and separation at a soft photocatalytic interface, *Adv. Mater.* 26 (2014) 4121–4126.

[63] Suyana Panneri, Priyanka Ganguly, Balagopal N. Nair, Abdul Azeez Peer Mohamed, Krishna Gopakumar Warrier, Unnikrishnan Nair, S. Hareesh, Copyrolysed C₃N₄/Ag/ZnO ternary heterostructure systems for enhanced adsorption and photocatalytic degradation of tetracycline, *Eur. J. Inorg. Chem.* (2016) 5068–5076.

[64] Xinyong Lu, Jun Xie, Shu-yuan Liu, Andrzej Adamski, Xiaobo Chen, Xin Li, Low-cost Ni₃B/Ni(OH)₂ as an ecofriendly hybrid cocatalyst for remarkably boosting photocatalytic H₂ production over g-C₃N₄ nanosheets, *ACS Sustain. Chem. Eng.* 6 (2018) 13140–13150.

[65] Y.X. Zeng, X. Liu, C.B. Liu, L.L. Wang, Y.C. Xia, S.Q. Zhang, S.L. Luo, Y. Pe, Scalable one-step production of porous oxygen-doped g-C₃N₄ nanorods with effective electron separation for excellent visible-light photocatalytic activity, *Appl. Catal. B* 224 (2018) 1–9.

[66] J. Ba, D.F. Rohlfing, A. Feldhoff, T. Brezesinski, I. Djerdj, M. Wark, M. Niederberger, Nonaqueous synthesis of uniform indium tin oxide nanocrystals and their electrical conductivity in dependence of the tin oxide concentration, *Chem. Mater.* 18 (2006) 2848–2854.

[67] Shao-Wen Cao, Xin-Feng Liu, Yu-Peng Yuan, Zhen-Yi Zhang, Yu-Sen Liao, Jun Fang, Say Chye Joachim Loo, Tze Chien Sum, Can Xue, Solar-to-fuels conversion over In₂O₃/g-C₃N₄ hybrid photocatalysts, *Appl. Catal. B* 147 (2014) 940–946.

[68] Chengyin Liu, Hongwei Huang, Wen Cui, Fan Dong, Yihe Zhang, Band structure engineering and efficient charge transport in oxygen substituted g-C₃N₄ for superior photocatalytic hydrogen evolution, *Appl. Catal. B* 230 (2018) 115–124.

[69] M.S. Sankar, Q. He, M. Morad, J. Pritchard, S.J. Freakley, J.K. Edwards, S.H. Taylor, D.J. Morgan, A.F. Carley, D.W. Knight, C.J. Kiely, G.J. Hutchings, Synthesis of stable ligand-free gold–palladium nanoparticles using a simple excess anion method, *ACS Nano* 6 (2012) 6600–6613.

[70] Ziyang Huo, Chia-kuang Tsung, Wenyu Huang, Xiaofeng Zhang, Peidong Yang, Subtwo nanometer single crystal Au nanowires, *Nano Lett.* 8 (2008) 2041–2044.

[71] Y.K. Mishra, G. Modi, V. Cretu, V. Postica, O. Lupan, T. Reimer, I. Paulowicz, V. Hrkac, W. Benecke, L. Kienle, R. Adelung, Direct growth of freestanding ZnO tetrapod networks for multifunctional applications in photocatalysis, UV photo-detection, and gas sensing, *ACS Appl. Mater. Interfaces* 7 (2015) 14303–14316.

[72] Junying Lin Yu Gao, Qingzhe Zhang, He Yu, Fu Ding, Baotong Xu, Yaguang Sun, Zhenhe Xu Facile synthesis of heterostructured YVO₄/g-C₃N₄/Ag photocatalysts with enhanced visible-light photocatalytic performance, *Appl. Catal. B* 224 (2018) 586–593.

[73] Sha-Sha Yi, Jun-Min Yan, Qing Jiang, Carbon quantum dot sensitized integrated Fe₂O₃@g-C₃N₄ core–shell nanoarray photoanode towards highly efficient water oxidation, *J. Mater. Chem. A* 6 (2018) 9839–9845.

[74] Mengqiao Hu, Zipeping Xing, Yan Cao, Zhenzi Li, Xu Yan, Ziyuan Xiu, Tianyu Zhao, Shilin Yang, Wei Zhou, Ti³⁺ self-doped mesoporous black TiO₂/SiO₂/g-C₃N₄ sheets heterojunctions as remarkable visible-light-driven photocatalysts, *Appl. Catal. B* 226 (2018) 499–508.

[75] Y. Xu, A.A.A. Schoonen, The absolute energy positions of conduction and valence bands of selected semiconducting minerals, *Am. Miner.* 85 (2000) 543–556.

[76] Jian Jin, Jiaoguo Yu, Daipeng Guo, Can Cui, Wingkei Ho, A hierarchical Z-Scheme CdS–WO₃ photocatalyst with enhanced CO₂ reduction activity, *Small* 11 (2015) 5262–5271.

[77] A.L. Luna, E. Novoseltceva, E. Louarn, P. Beaunier, E. Kowalska, B. Ohtani, M.A. Valenzuela, H. Remita, C. Colbeau-Justin, Synergistic effect of Ni and Au nanoparticles synthesized on titania particles for efficient photocatalytic hydrogen production, *Appl. Catal. B* 191 (2016) 18–28.

[78] M.G. Méndez-Medrano, E. Kowalska, A. Lehoux, A. Herissan, B. Ohtani, S. Rau, C. Colbeau-Justin, J.L. Rodríguez-López, H. Remita, Surface modification of TiO₂ with Au nanoclusters for efficient water treatment and hydrogen generation under visible light, *J. Phys. Chem. C* 120 (2016) 25010–25022.

[79] C. Marchal, A. Piquet, M. Behr, T. Cottineau, V. Papaefthimiou, V. Keller, V. Caps, Activation of solid grinding-derived Au/TiO₂ photocatalysts for solar H₂ production

from water-methanol mixtures with low alcohol content, *J. Catal.* 352 (2017) 22–34.

[80] F.-W. Chang, H.-Y. Yu, L. Selva Roselin, H.-C. Yang, Production of hydrogen via partial oxidation of methanol over Au/TiO₂ catalysts, *Appl. Catal. A Gen.* 290 (2005) 138–147.

[81] P. Konova, A. Naydenov, C. Venkov, D. Mehandjiev, D. Andreeva, T. Tabakova, Activity and deactivation of Au/TiO₂ catalyst in CO oxidation, *J. Mol. Catal. A Chem.* 213 (2004) 235–240.

[82] Jean-Philippe Sylvestre, Suzie Poulin, Andrei V. Kabashin, Edward Sacher, Michel Meunier, John H.T. Luong, Surface chemistry of gold nanoparticles produced by laser ablation in aqueous media, *J. Phys. Chem. B* 108 (2004) 16864–16869.

[83] V. Matolin, M. Cabala, I. Matolinova, M. Skoda, J. Libra, M. Vaclavu, K.C. Prince, T. Skala, H. Yoshikawa, Y. Yamashita, S. Ueda, K. Kobayashi, Au⁺ and Au³⁺ ions in CeO₂ rf-sputtered thin films, *J. Phys. D Appl. Phys.* 42 (2009) 7 115301.